DC spinmotive force from microwave-active resonant dynamics of a skyrmion crystal under a tilted magnetic field

Tatsuya Koide,[1] Akihito Takeuchi,[1] and Masahito Mochizuki[2,3]
[1]*Department of Physics and Mathematics, Aoyama Gakuin University, Sagamihara, Kanagawa 229-8558, Japan*
[2]*Department of Applied Physics, Waseda University, Okubo, Shinjuku-ku, Tokyo 169-8555, Japan*
[3]*PRESTO, Japan Science and Technology Agency, Kawaguchi, Saitama 332-0012, Japan*

(Received 17 April 2019; published 3 July 2019)

We theoretically show that a temporally oscillating spin-driven electromotive force or voltage with a large DC component can be generated by exciting microwave-active spin-wave modes of a skyrmion crystal confined in a quasi-two-dimensional magnet under a tilted magnetic field. The DC component and the AC amplitude of the oscillating electric voltage is significantly enhanced when the microwave frequency is tuned to an eigenfrequency of the peculiar spin-wave modes of the skyrmion crystal called "rotation modes" and the "breathing mode," whereas the sign of the DC component depends on the microwave polarization and on the spin-wave mode. These results provide an efficient means to convert microwaves to a DC electric voltage by using skyrmion-hosting magnets and to switch the sign of the voltage via tuning the microwave frequency, which are important capabilities for spintronic devices.

DOI: 10.1103/PhysRevB.100.014408

I. INTRODUCTION

Dynamic coupling between conduction electrons and noncollinear magnetic textures in magnets gives rise to a variety of physical phenomena, which have attracted significant research interest from the viewpoints of both fundamental science and technical applications. The spin-driven electromotive force (i.e., an emergent electric field induced by magnetization dynamics) is one of the most important of these phenomena [1,2]. It was proposed theoretically that noncollinear magnetizations produce a spatially inhomogeneous effective vector potential acting on conduction electrons via the *s*-*d* exchange coupling between conduction-electron spins and the magnetization. A temporal variation of this effective vector potential due to the dynamics of the magnetization induces an effective electromotive force that acts on the conduction electrons, which is referred to as the spinmotive force. The spinmotive force can also be interpreted as the inverse effect of the spin-transfer torque mechanism (see Fig. 1). The spinmotive force is expressed by

$$E_\mu(\boldsymbol{r},t) = \frac{\hbar}{2e}\boldsymbol{m}\cdot(\partial_\mu \boldsymbol{m}\times\partial_t \boldsymbol{m}) \quad (\mu = x, y), \tag{1}$$

where $\boldsymbol{m}(\boldsymbol{r},t)$ is the normalized classical magnetization vector. This formula explicitly indicates that the magnetization must vary both spatially and temporally to produce the spinmotive force. Several experimental reports discuss the generation and observation of the spinmotive force in ferromagnetic domain walls and magnetic vortices [3,4].

Recent theoretical work revealed that hexagonally packed skyrmions in a skyrmion crystal exhibit peculiar spin-wave modes at microwave frequencies, in which the skyrmions rotate uniformly in a counterclockwise or clockwise sense (the rotation modes) or uniformly expand and shrink in an oscillatory manner (the breathing mode) [5,6]. Subsequently, Ohe and colleagues showed numerically that the spin-driven electric voltage (the so-called spin voltage) can be generated from these microwave-active spin-wave modes of a magnetic skyrmion crystal [7,8]. An advantage of using a skyrmion crystal to generate the spin voltage is that the periodically aligned skyrmions in the skyrmion crystal work as batteries connected in series, which give a large electric voltage by summing each contribution. However, the spin voltage oscillates temporally and is, more specifically, a pure AC voltage with an average of zero. For certain spintronics applications, DC electric voltages are preferable. One possible way to obtain a DC voltage is to use an AC-DC transducer to convert the AC voltage to a DC voltage. However, this approach requires fabricating complicated devices. Moreover, we cannot avoid reduction of the voltage in the conversion process, which can be a critical problem because the spin voltage is originally very small. Therefore, a simple technique to generate a DC spin voltage is highly desired.

In this paper, we show theoretically that an oscillating spin voltage with a large DC component can be generated by exciting the microwave-active spin-wave modes of skyrmion crystal on a quasi-two-dimensional thin-plate magnet under an external magnetic field $\boldsymbol{H}_{\rm ex}$ tilted with respect to the perpendicular direction. By numerically solving the Landau-Lifshitz-Gilbert (LLG) equation, we trace the dynamics of magnetization in the skyrmion crystal activated by a microwave magnetic field $\boldsymbol{H}^\omega$. We use the results of the simulation of the magnetization dynamics to calculate the spatiotemporal profiles of the spinmotive force and the temporal profiles of the spin voltage. The results show that the DC component and the AC amplitude of the temporally oscillating electric voltage increase significantly when the frequency of the microwave is tuned to an eigenfrequency of the spin-wave modes, which converts the microwave power to a DC voltage with high efficiency using a skyrmion-hosting magnet. The

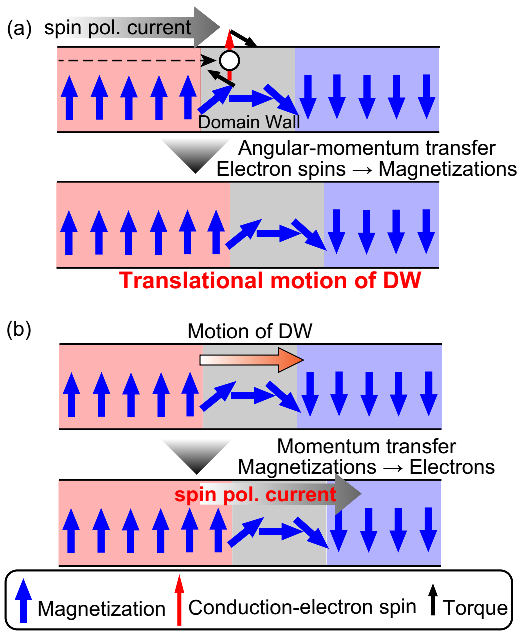

FIG. 1. (a) Schematics of the spin-transfer torque mechanism. Angular momentum transfer from conduction-electron spins of an injected spin-polarized current to magnetizations constituting a noncollinear magnetic texture drives the translational motion of the magnetic texture. (b) Schematics of spin-driven electromotive force, the so-called spinmotive force. Momentum transfer from a driven noncollinear magnetic texture to the conduction electrons via exchange coupling causes an effective electromotive force acting on the conduction electrons, resulting in the generation of spin-polarized electric currents. Here we consider a domain wall in a ferromagnetic nanowire as an example of the noncollinear magnetic texture.

results also show that the sign of the DC voltage depends on the excited spin-wave modes, which indicates that the sign of the voltage can be switched by tuning the microwave frequency. Our finding will be useful for technical applications in spintronics devices.

II. MODEL AND METHOD

We start with a classical Heisenberg model on a square lattice to describe a thin-plate specimen of the skyrmion-hosting magnet. The model contains the ferromagnetic-exchange interaction, the Dzyaloshinskii-Moriya (DM) interaction, and the Zeeman interaction with an external magnetic field $\boldsymbol{H}_{\rm ex} = (H_x, 0, H_z)$ [9]. The Hamiltonian is given by [10]

$$\begin{aligned}\mathcal{H}_0 = & -J\sum_i (\boldsymbol{m}_i \cdot \boldsymbol{m}_{i+\hat{x}} + \boldsymbol{m}_i \cdot \boldsymbol{m}_{i+\hat{y}}) \\ & -D\sum_i (\boldsymbol{m}_i \times \boldsymbol{m}_{i+\hat{x}} \cdot \hat{\boldsymbol{x}} + \boldsymbol{m}_i \times \boldsymbol{m}_{i+\hat{y}} \cdot \hat{\boldsymbol{y}}) \\ & -\boldsymbol{H}_{\rm ex} \cdot \sum_i \boldsymbol{m}_i, \end{aligned} \tag{2}$$

where $\boldsymbol{m}_i$ is the normalized magnetization vector on the ith lattice site. We use $J = 1$ as the energy units and set $D/J = 0.27$. The vertical component of $\boldsymbol{H}_{\rm ex}$ is fixed at

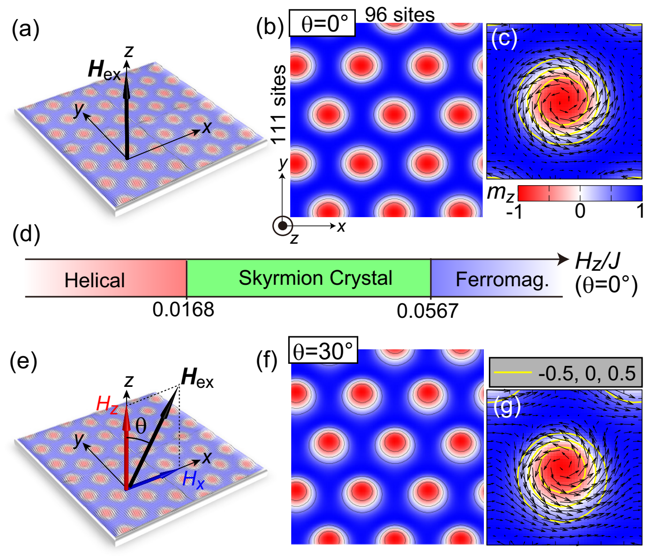

FIG. 2. Thin-plate specimen of a chiral-lattice magnet hosting a skyrmion crystal under (a) a perpendicular and (e) tilted external magnetic field $\boldsymbol{H}_{\rm ex} = (H_z \tan\theta, 0, H_z)$ with tilting angles of $\theta = 0^\circ$ and $\theta \neq 0^\circ$, respectively. Skyrmion crystal under (b) the perpendicular and (f) tilted magnetic field $\boldsymbol{H}_{\rm ex}$ with $\theta = 0^\circ$ and $\theta = 30^\circ$, respectively. Magnetization configuration of a skyrmion constituting the skyrmion crystal under (c) a perpendicular and (g) tilted magnetic field $\boldsymbol{H}_{\rm ex}$. (d) Theoretical phase diagram of the spin model given by Eq. (2) at $T = 0$ as a function of the out-of-plane component of $\boldsymbol{H}_{\rm ex}$ when $\theta = 0^\circ$.

$H_z = 0.036$, whereas the in-plane component is $H_x = H_z \tan\theta$, with θ being the tilting angle of $\boldsymbol{H}_{\rm ex}$.

The lattice spacing of a skyrmion crystal, i.e., the distance between cores of neighboring skyrmions, is determined by competition between the DM interaction and the ferromagnetic exchange interaction, which favor rotating and parallel magnetization alignments, respectively. A stronger DM interaction causes rapid rotation of the magnetizations and, consequently, a smaller skyrmion size. Because $\phi \sim D/(\sqrt{2}J)$ holds for the magnetization rotation angle ϕ, the spatial period in the skyrmion crystal becomes $\lambda_{\rm m} \sim 2\pi a/\phi$ when $\boldsymbol{H}_{\rm ex} = 0$, where a is the lattice constant. Even when $\boldsymbol{H}_{\rm ex}$ is finite, this spatial period does not change very much, although the magnetization rotation is no longer uniform. Therefore, the ratio $D/J = 0.27$ gives $\lambda_{\rm m} \sim 18$ nm if we assume a typical lattice constant of $a = 0.5$ nm, which corresponds to the experimentally observed skyrmion size in MnSi [11,12]. When the external magnetic field $\boldsymbol{H}_{\rm ex}$ is applied perpendicular to the thin-plate plane [i.e., $\boldsymbol{H}_{\rm ex} = (0, 0, H_z)$] as shown in Fig. 2(a), the skyrmion-crystal phase with hexagonally packed skyrmions [Fig. 2(b)] appears when the field strength H_z is moderate [13–16]. The emergence of a skyrmion crystal was predicted theoretically [17–19] and has indeed been observed experimentally [11,12,20–23]. In this case, each skyrmion in the skyrmion crystal has a circular symmetry, as shown in Fig. 2(c). Figure 2(d) shows a theoretical phase diagram of this spin model given by Eq. (2) at $T = 0$ as a function of the magnetic-field strength H_z when $\boldsymbol{H}_{\rm ex} = (0, 0, H_z)$. This phase diagram exhibits the skyrmion-crystal phase in a region of

TABLE I. Unit conversion table for $J = 1$ meV.

	Dimensionless quantity	Corresponding value with units
Exchange interaction	$J = 1$	$J = 1$ meV
Time	$t = 1$	$\hbar/J = 0.66$ ps
Frequency $f = \omega/2\pi$	$\omega = 1$	$J/h = 241$ GHz
Magnetic field	$H = 1$	$J/g\mu_B = 8.64$ T

moderate field strength sandwiched by the helical phase and the field-polarized ferromagnetic phase. The unit conversions for $J = 1$ meV are summarized in Table I. When $J = 1$ meV, $H_z = 1$ corresponds to $\sim$8.64 T. Therefore, the threshold fields of $H_{c1} = 0.0168$ and $H_{c2} = 0.0567$ in this theoretical phase diagram correspond to 0.145 and 0.49 T, respectively. These values coincide well with the experimentally observed threshold fields of $\sim$0.15 and $\sim$0.45 T for MnSi at low temperatures [12].

The skyrmion-crystal phase survives even when the magnetic field $\boldsymbol{H}_{\rm ex}$ is tilted with respect to the perpendicular direction [see Fig. 2(e)] [24]. Figure 2(f) shows a skyrmion crystal under a magnetic field $\boldsymbol{H}_{\rm ex}$ tilted towards the x direction at a tilting angle of $\theta = 30^\circ$, and Fig. 2(g) displays the magnetization configuration of a skyrmion in this skyrmion crystal, which has a disproportionate weight in the distribution of the m_z components slanted from its center.

We simulate the dynamics of the magnetization in the skyrmion-crystal state activated by a microwave magnetic field $\boldsymbol{H}^\omega$ by numerically solving the LLG equation using the fourth-order Runge-Kutta method. The LLG equation

$$\frac{d\boldsymbol{m}_i}{dt} = -\gamma \boldsymbol{m}_i \times \boldsymbol{H}_i^{\rm eff} + \frac{\alpha_{\rm G}}{m}\boldsymbol{m}_i \times \frac{d\boldsymbol{m}_i}{dt}. \tag{3}$$

The first term on the right-hand side is the gyrotropic term and describes the precessional motion of magnetizations $\boldsymbol{m}_i$ around the effective local magnetic field $\boldsymbol{H}_i^{\rm eff}$. The second term is the Gilbert-damping term introduced phenomenologically to describe the dissipation of the gyration energy. The Gilbert-damping coefficient is fixed at $\alpha_{\rm G} = 0.02$ for calculations of the microwave absorption spectra shown in Fig. 3 to precisely evaluate the eigenfrequencies of the skyrmion spin-wave modes, while it is fixed at $\alpha_{\rm G} = 0.04$ for calculations of the spinmotive force to evaluate its realistic values for MnSi. The effective magnetic field $\boldsymbol{H}_i^{\rm eff}$ is calculated from the Hamiltonian $\mathcal{H} = \mathcal{H}_0 + \mathcal{H}'(t)$ as follows:

$$\boldsymbol{H}_i^{\rm eff} = -\frac{1}{\gamma\hbar}\frac{\partial \mathcal{H}}{\partial \boldsymbol{m}_i}. \tag{4}$$

Here $\mathcal{H}_0$ is the model Hamiltonian given by Eq. (2), whereas $\mathcal{H}'(t)$ is the coupling between magnetizations and a time-dependent magnetic field or a microwave magnetic field $\boldsymbol{H}(t)$ in the form

$$\mathcal{H}'(t) = -\boldsymbol{H}(t)\cdot\sum_i \boldsymbol{m}_i. \tag{5}$$

The initial magnetic configurations of a skyrmion crystal are prepared by Monte Carlo thermalization at low temperatures and by further relaxing them in the LLG simulation without applying a microwave magnetic field. We simulate the microwave-driven magnetization dynamics by applying a microwave field to a thus-obtained sufficiently converged skyrmion-crystal configuration.

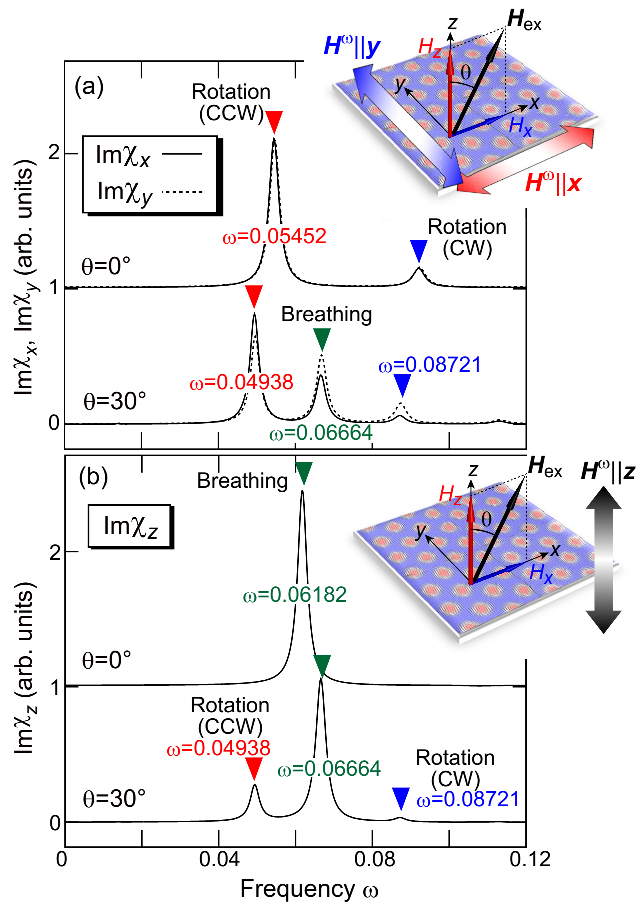

FIG. 3. Calculated imaginary parts of the dynamical magnetic susceptibilities Imχ_μ ($\mu = x, y, z$) of the skyrmion crystal confined in the two-dimensional system under perpendicular ($\theta = 0^\circ$) and tilted ($\theta = 30^\circ$) magnetic fields $\boldsymbol{H}_{\rm ex}$ with $H_z = 0.036$ as functions of the microwave frequency ω. (a) Imχ_x and Imχ_y for the in-plane microwave polarization with $\boldsymbol{H}^\omega \parallel \boldsymbol{x}, \boldsymbol{y}$. (b) Im$\chi_z$ for the out-of-plane microwave polarization with $\boldsymbol{H}^\omega \parallel \boldsymbol{z}$. The dominant mode component and the value of the eigenfrequency are shown at each peak position.

Using the calculated spatiotemporal dynamics of excited magnetization $\boldsymbol{m}_i$, we calculate the spatiotemporal profile of the spinmotive force $\boldsymbol{E}$. For the numerical calculation, it is convenient to rewrite Eq. (1) in discretized form as

$$E_{\mu,i}(t) = \frac{\hbar}{2e}\boldsymbol{m}_i(t)\left(\frac{\boldsymbol{m}_{i+\hat{\mu}}(t) - \boldsymbol{m}_{i-\hat{\mu}}(t)}{2a} \times \frac{\boldsymbol{m}_i(t+\Delta t) - \boldsymbol{m}_i(t-\Delta t)}{2\Delta t}\right), \tag{6}$$

where $\mu = x, y$ and a (=5 Å) is the lattice constant. We also calculate time profiles of the spin voltage by numerically solving the Poisson equation. All the calculations are done using a system of $N = 96 \times 111$ sites with periodic boundary conditions.

To identify the spin-wave modes and their eigenfrequencies, we first calculate the dynamical magnetic susceptibility,

$$\chi_\mu(\omega) = \frac{\Delta M_\mu(\omega)}{H_\mu(\omega)} \quad (\mu = x, y, z), \tag{7}$$

where $H_\mu(\omega)$ and $\Delta M_\mu(\omega)$ are the Fourier transforms of the time-dependent magnetic field $\boldsymbol{H}(t)$ and the simulated time profile of the net magnetization $\Delta\boldsymbol{M}(t) = \boldsymbol{M}(t) - \boldsymbol{M}(0)$, with $\boldsymbol{M}(t) = \frac{1}{N}\sum_{i=1}^{N} \boldsymbol{m}_i(t)$. In this calculation, we use a short rectangular pulse for $\boldsymbol{H}(t)$ whose components are given by

$$H_\mu(t) = \begin{cases} H_{\text{pulse}} & 0 \leqslant t \leqslant 1, \\ 0 & \text{otherwise}, \end{cases} \tag{8}$$

where $t = (J/\hbar)\tau$ is the dimensionless time, with τ being the real time. An advantage of using a short pulse is that the Fourier component $H_\mu(\omega)$ becomes constant, being independent of ω up to first order in $\omega\Delta t$ for a sufficiently short duration Δt with $\omega\Delta t \ll 1$. The Fourier component is

$$H_\mu(\omega) = \int_0^{\Delta t} H_{\text{pulse}} e^{i\omega t} dt = \frac{H_{\text{pulse}}}{i\omega}(e^{i\omega\Delta t} - 1) \sim H_{\text{pulse}}\Delta t. \tag{9}$$

Consequently, we obtain the relationship $\chi_\mu(\omega) \propto \Delta M_\mu(\omega)$.

III. RESULTS

Figures 3(a) and 3(b) show the calculated microwave absorption spectra (i.e., the imaginary parts of the dynamical magnetic susceptibilities Im χ_μ ($\mu = x, y, z$) under perpendicular ($\theta = 0^\circ$) and tilted ($\theta = 30^\circ$) magnetic fields $\boldsymbol{H}_{\text{ex}}$ as functions of microwave frequency $\omega(=2\pi f)$. More specifically, Fig. 3(a) shows the calculated microwave absorption spectra for the in-plane microwave polarization with $\boldsymbol{H}^\omega \parallel \boldsymbol{x}, \boldsymbol{y}$ (Imχ_x and Imχ_y), whereas Fig. 3(b) shows the calculated microwave absorption spectra for the out-of-plane microwave polarization with $\boldsymbol{H}^\omega \parallel \boldsymbol{z}$ (Imχ_z). Here we fix $H_z = 0.036$ for the calculations. A dominant component of the oscillation mode is indicated at each peak position. Figure 3(a) shows that whereas only two rotation modes can be excited by the in-plane microwave field $\boldsymbol{H}^\omega \parallel \boldsymbol{x}, \boldsymbol{y}$ under a perpendicular magnetic field $\boldsymbol{H}_{\text{ex}}$ ($\theta = 0^\circ$), the breathing mode also becomes active when the magnetic field $\boldsymbol{H}_{\text{ex}}$ is tilted. Similarly, Fig. 3(b) indicates that the rotation modes can be excited by the out-of-plane microwave field $\boldsymbol{H}^\omega \parallel \boldsymbol{z}$ as well under the tilted magnetic field $\boldsymbol{H}_{\text{ex}}$, although only the breathing mode is active for $\boldsymbol{H}^\omega \parallel \boldsymbol{z}$ under the perpendicular magnetic field $\boldsymbol{H}_{\text{ex}}$.

Comparing the spectra in Fig. 3(a) with those in Fig. 3(b), we find that three spin-wave modes excited by $\boldsymbol{H}^\omega \parallel \boldsymbol{x}, \boldsymbol{y}$ have identical eigenfrequencies with three corresponding modes excited by $\boldsymbol{H}^\omega \parallel \boldsymbol{z}$, indicating that both the in-plane microwave fields $\boldsymbol{H}^\omega \parallel \boldsymbol{x}, \boldsymbol{y}$ and the out-of-plane microwave field $\boldsymbol{H}^\omega \parallel \boldsymbol{z}$ excite the same modes under the tilted magnetic field $\boldsymbol{H}_{\text{ex}}$. Although the spectra here are calculated for the Bloch-type skyrmion crystal, the Néel-type and the antivortex-type skyrmion crystals produce the same spectra.

Figures 4(a)–4(c) show time profiles of the spin voltage V_x measured between the left and right edges of the system along the x axis under application of a perpendicular magnetic field $\boldsymbol{H}_{\text{ex}}$ with $\theta = 0^\circ$ for various spin-wave modes, i.e., the counterclockwise rotation mode excited by $\boldsymbol{H}^\omega \parallel \boldsymbol{x}$, the counterclockwise rotation mode excited by $\boldsymbol{H}^\omega \parallel \boldsymbol{y}$, and the breathing mode excited by $\boldsymbol{H}^\omega \parallel \boldsymbol{z}$, respectively. The dots are the results of the numerical simulations, and the solid lines are fits using the following formula of a forced oscillation with damping:

$$V_\mu = V_\mu^{\text{DC}} + V_\mu^{\text{AC}}(1 - e^{-t/\tau}) \sin\omega t, \tag{10}$$

with $\mu = x$. Here V_μ^{DC}, V_μ^{AC}, ω (=$2\pi f$), and τ are the DC component, the AC amplitude, the angular frequency, and the decay rate of the induced temporally oscillating spin voltage, respectively. Here the simulations were done for the microwave amplitude of $H^\omega = 3 \times 10^{-3}$ ($H^\omega = 2 \times 10^{-3}$) for the in-plane (out-of-plane) polarized microwaves $\boldsymbol{H}^\omega \parallel \boldsymbol{x}, \boldsymbol{y}$ ($\boldsymbol{H}^\omega \parallel \boldsymbol{z}$), which corresponds to ~26 mT (~17.3 mT) when $J = 1$ meV. When the magnetic field $\boldsymbol{H}_{\text{ex}}$ is perpendicular to the thin-plate-shaped sample, pure AC voltages with zero DC component are obtained for the rotation mode, as seen in Figs. 4(a) and 4(b), whereas the spin voltage is exactly zero for the breathing mode, as seen in Fig. 4(c). For example, the data in Fig. 4(a) are well fit by Eq. (10) with $V_x^{\text{DC}} = 0\ \mu$V and $V_x^{\text{AC}} = 4.24\ \mu$V.

In Figs. 4(d) and 4(e), spatial maps of the electromotive force vectors $\boldsymbol{E}(\boldsymbol{r}, t)$ at selected moments are shown by arrows. Here the colors indicate the out-of-plane magnetization component m_z to visualize the temporally varying skyrmion shape at each moment in the spin-wave excitation. Figure 4(d) shows that the $\boldsymbol{E}$-field vectors circulate together with the rotating skyrmion in the counterclockwise rotation mode. The observed pure AC voltage is attributed to this symmetric circulation of the $\boldsymbol{E}$-field vectors. On the contrary, Fig. 4(e) shows that the circularly symmetric source and sink of the $\boldsymbol{E}$ fields oscillate together with the oscillatory expansion and shrinkage of the skyrmion in the breathing mode. The observed exact-zero electric voltage is attributed to the radially distributed $\boldsymbol{E}$-field vectors with a circular symmetry.

Conversely, Figs. 4(f)–4(h) show the temporal profiles of spin voltage V_x under application of a tilted magnetic field $\boldsymbol{H}_{\text{ex}}$ with $\theta = 30^\circ$. Figures 4(f) and 4(g) show that the center of mass of the oscillation of V_x shifts downwards, indicating the emergence of a finite DC component V_x^{DC}. Surprisingly, the oscillating electric voltage with a large DC component also appears for the breathing mode, as seen in Fig. 4(h), which is in striking contrast to the pure AC voltage with zero DC component observed under the perpendicular magnetic field $\boldsymbol{H}^{\text{ex}}$. Note that the DC component V_x^{DC} is negative in the former cases in Figs. 4(f) and 4(g), whereas it is positive in the latter case in Fig. 4(h).

Figures 5(a) and 5(b) show the calculated microwave-frequency dependence of the AC amplitude of the spin voltage V_μ^{AC} ($\mu = x, y$) for the in-plane microwave polarizations $\boldsymbol{H}^\omega \parallel \boldsymbol{x}, \boldsymbol{y}$ and the out-of-plane microwave polarization $\boldsymbol{H}^\omega \parallel \boldsymbol{z}$, respectively. Note that $\boldsymbol{H}^\omega \parallel \boldsymbol{x}$ and $\boldsymbol{H}^\omega \parallel \boldsymbol{y}$ give slightly different behaviors even though both are similarly in plane polarized because the symmetry between the x and y directions is broken by the in-plane magnetic field applied along the x axis. We fixed the amplitude of the applied microwave field at $H^\omega = 0.6 \times 10^{-3}$ in the simulations. These plots indicate that the

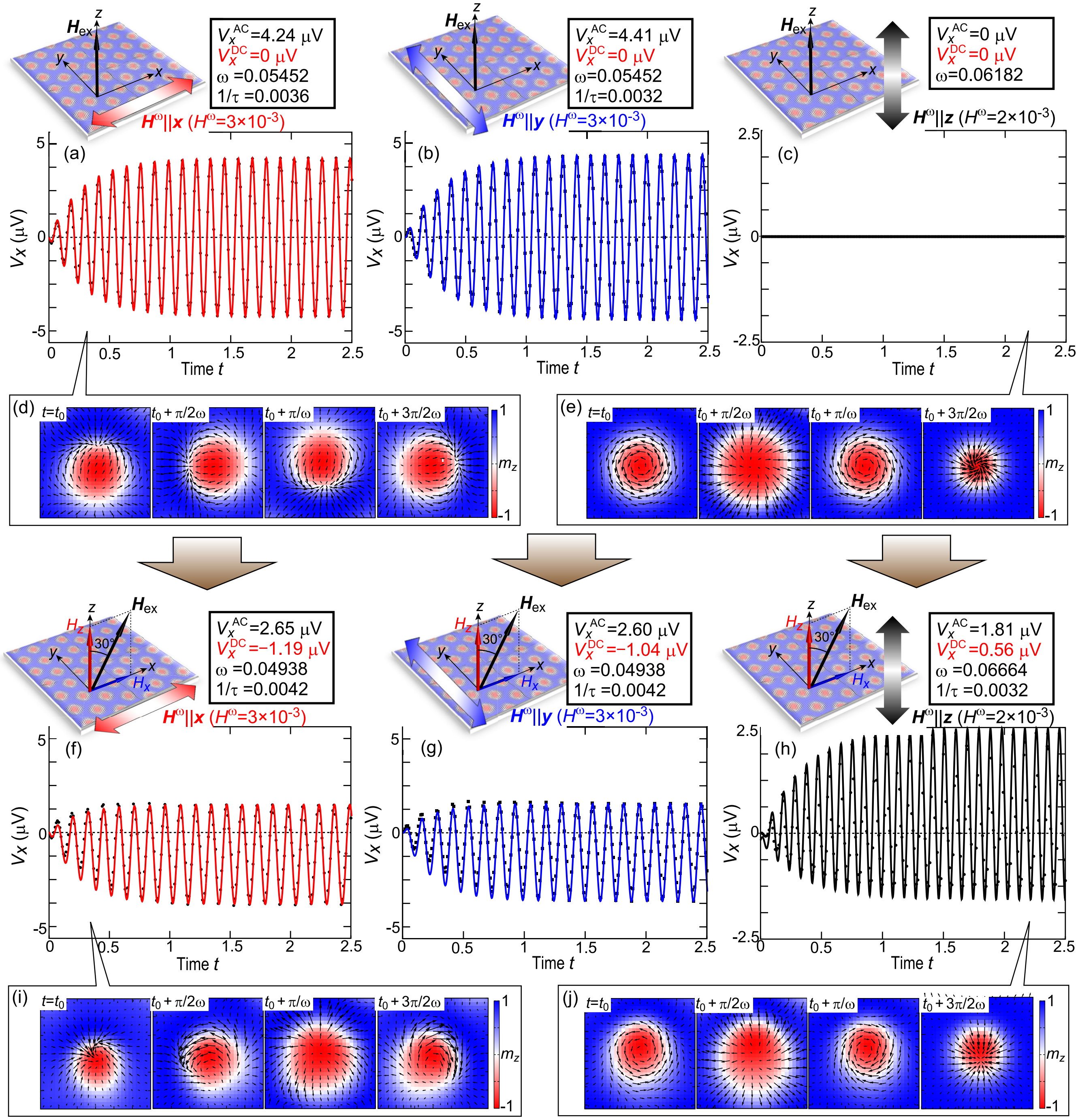

FIG. 4. Calculated time profiles of spin voltages induced by the microwave-active spin-wave modes of a skyrmion crystal confined in a thin-plate magnet under (a)–(c) a perpendicular and (f)–(h) tilted magnetic field $\boldsymbol{H}_{\rm ex}$ with $\theta = 0^\circ$ and $\theta = 30^\circ$, respectively, and $H_z = 0.036$ for various microwave polarizations and frequencies. (a) and (f) $\boldsymbol{H}^\omega \parallel \boldsymbol{x}$ with a frequency fixed at the eigenfrequency of the counterclockwise rotation mode, (b) and (g) $\boldsymbol{H}^\omega \parallel \boldsymbol{y}$ with a frequency fixed at the eigenfrequency of the counterclockwise rotation mode, and (c) and (h) $\boldsymbol{H}^\omega \parallel \boldsymbol{z}$ with a frequency fixed at the eigenfrequency of the breathing mode. The amplitude of the applied microwave is fixed at $H^\omega = 3 \times 10^{-3}$ for the in-plane polarized microwave $\boldsymbol{H}^\omega \parallel \boldsymbol{x}, \boldsymbol{y}$ in (a), (b), (f), and (g), whereas it is fixed at $H^\omega = 2 \times 10^{-3}$ for the out-of-plane polarized microwave $\boldsymbol{H}^\omega \parallel \boldsymbol{z}$ in (c) and (h). Here the values of the AC amplitude $V_x^{\rm AC}$, the DC component $V_x^{\rm DC}$, the angular frequency $\omega(=2\pi f)$, and the decay rate τ of the generated time-dependent spin voltage are shown for each case, as obtained by fitting the simulation results (see text). The results show that the DC voltage $V_x^{\rm DC}$ is always zero under the perpendicular magnetic field $\boldsymbol{H}_{\rm ex}$, whereas it becomes finite when the magnetic field $\boldsymbol{H}_{\rm ex}$ is tilted. (d), (e), (i), and (j) Snapshots of the spatial distribution of the spinmotive force (arrows) at selected times. The out-of-plane magnetization components m_z are also shown in color to facilitate the visualization of the temporally varying skyrmion shape.

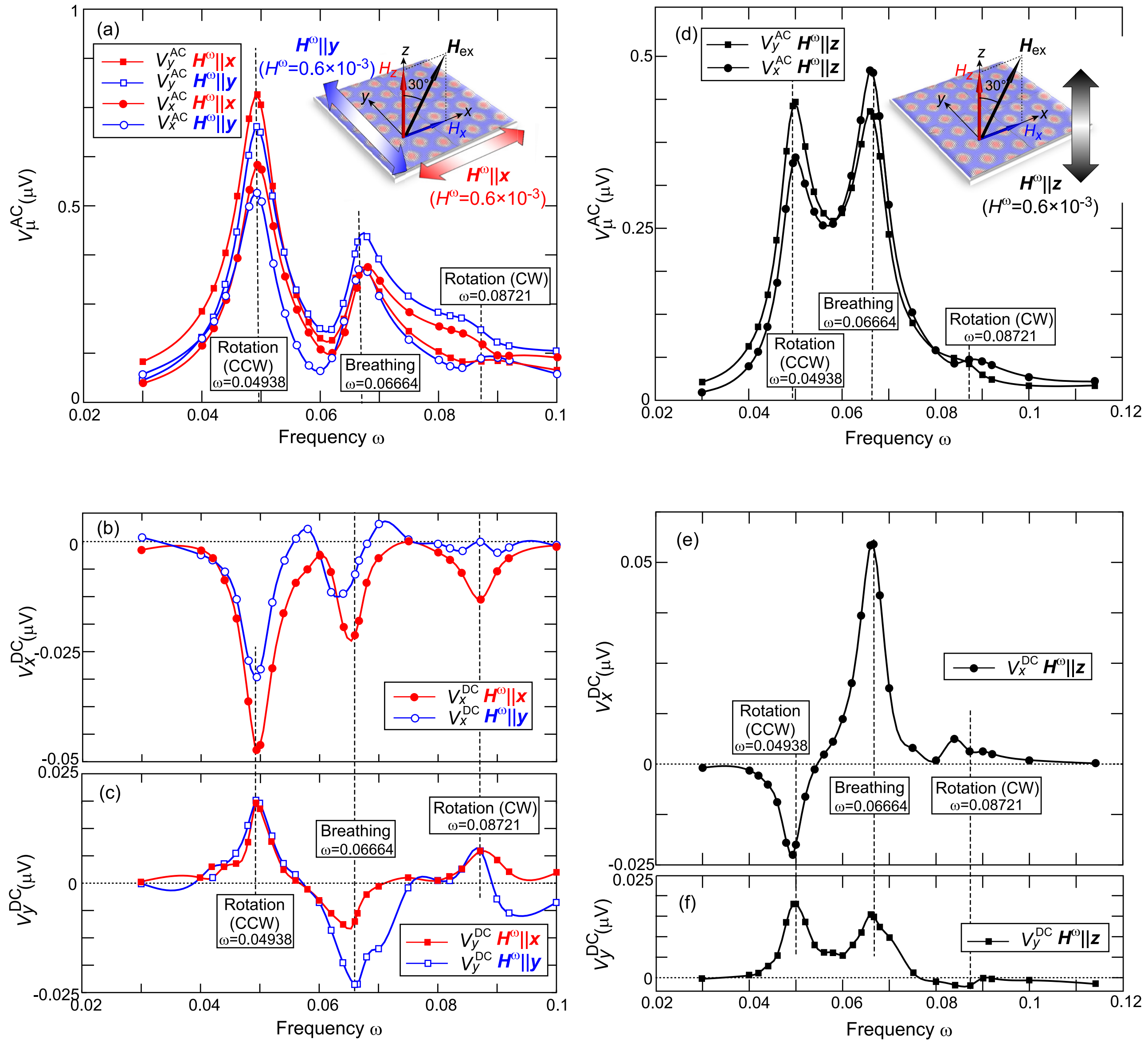

FIG. 5. Calculated microwave-frequency dependence of the AC amplitude V_μ^{AC} and the DC component V_μ^{DC} ($\mu = x, y$) of the spin voltage under application of a tilted magnetic field $\boldsymbol{H}_{ex}$ with $\theta = 30^\circ$ and $H_z = 0.036$ for the (a)–(c) in-plane and (d)–(f) out-of-plane microwave polarizations $\boldsymbol{H}^\omega \parallel \boldsymbol{x}, \boldsymbol{y}$ and $\boldsymbol{H}^\omega \parallel \boldsymbol{z}$, respectively, i.e., (a) and (d) V_x^{AC} and V_y^{AC}, (b) and (e) V_x^{DC}, and (c) and (f) V_y^{DC}. Here the amplitude of the applied microwave is fixed at $H^\omega = 0.6 \times 10^{-3}$ for all simulations.

AC amplitude is enhanced and peaks at eigenfrequencies of the spin-wave modes. In particular, significant enhancement occurs when the microwave frequency is tuned to the eigenfrequency of the counterclockwise rotation mode and that of the breathing mode.

Conversely, Figs. 5(c)–5(f) show the microwave-frequency dependence of the DC components of the spin voltage V_μ^{DC} ($\mu = x, y$) for different microwave polarizations. Specifically, Fig. 5(c) shows V_x^{DC} for $\boldsymbol{H}^\omega \parallel \boldsymbol{x}, \boldsymbol{y}$, Fig. 5(d) shows V_y^{DC} for $\boldsymbol{H}^\omega \parallel \boldsymbol{x}, \boldsymbol{y}$, Fig. 5(e) shows V_x^{DC} for $\boldsymbol{H}^\omega \parallel \boldsymbol{z}$, and Fig. 5(f) shows V_y^{DC} for $\boldsymbol{H}^\omega \parallel \boldsymbol{z}$. The microwave amplitude was again fixed at $H^\omega = 0.6 \times 10^{-3}$ for these simulations. The results show that the DC component is enhanced at the eigenfrequencies of the spin-wave modes. Moreover, the sign of V_μ^{DC} depends on the spin-wave mode. For example, the sign variation is apparent for the three spin-wave modes in the profile of V_y^{DC} for $\boldsymbol{H}^\omega \parallel \boldsymbol{x}, \boldsymbol{y}$ [Fig. 5(d)] and in the profile of V_x^{DC} for $\boldsymbol{H}^\omega \parallel z$ [Fig. 5(e)], which indicates that the sign of the voltage depends strongly on the mode.

The results also show that the sign of V_μ^{DC} depends on the microwave polarization, even when the same spin-wave mode is excited. For example, for the breathing mode, both V_x^{DC} and V_y^{DC} are negative for the in-plane microwave polarization $\boldsymbol{H}^\omega \parallel \boldsymbol{x}, \boldsymbol{y}$, as seen in Figs. 5(c) and 5(d), but are positive for the out-of-plane microwave polarization $\boldsymbol{H}^\omega \parallel \boldsymbol{z}$, as seen in Figs. 5(e) and 5(f). Finally, note that a large DC voltage is obtained for the counterclockwise rotation mode excited by $\boldsymbol{H}^\omega \parallel \boldsymbol{x}, \boldsymbol{y}$ and for the breathing mode excited by $\boldsymbol{H}^\omega \parallel \boldsymbol{z}$, which indicates that these sets of microwave polarization and the spin-wave mode are suitable for efficient conversion of

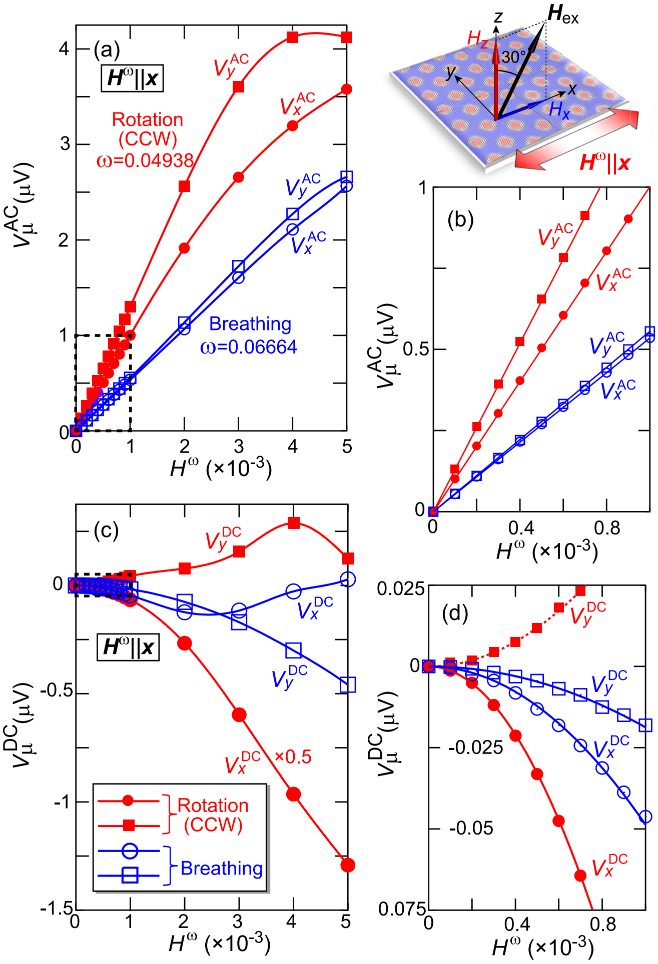

FIG. 6. Calculated microwave-amplitude dependence of (a) the AC amplitudes V_x^{AC} and V_y^{AC} and (c) the DC components V_x^{DC} and V_y^{DC} of the spin voltages, respectively, for the counterclockwise rotation mode and the breathing mode excited by the in-plane microwave field $\boldsymbol{H}^\omega \parallel \boldsymbol{x}$ under application of a tilted magnetic field $\boldsymbol{H}_{\rm ex}$ with $\theta = 30^\circ$ and $H_z = 0.036$. (b) and (d) Magnified view of the area indicated by the dashed rectangle in (a) and (c), respectively. The frequency of the applied microwave field is fixed at $\omega = 0.04938$ for the counterclockwise rotation mode and at $\omega = 0.0664$ for the breathing mode.

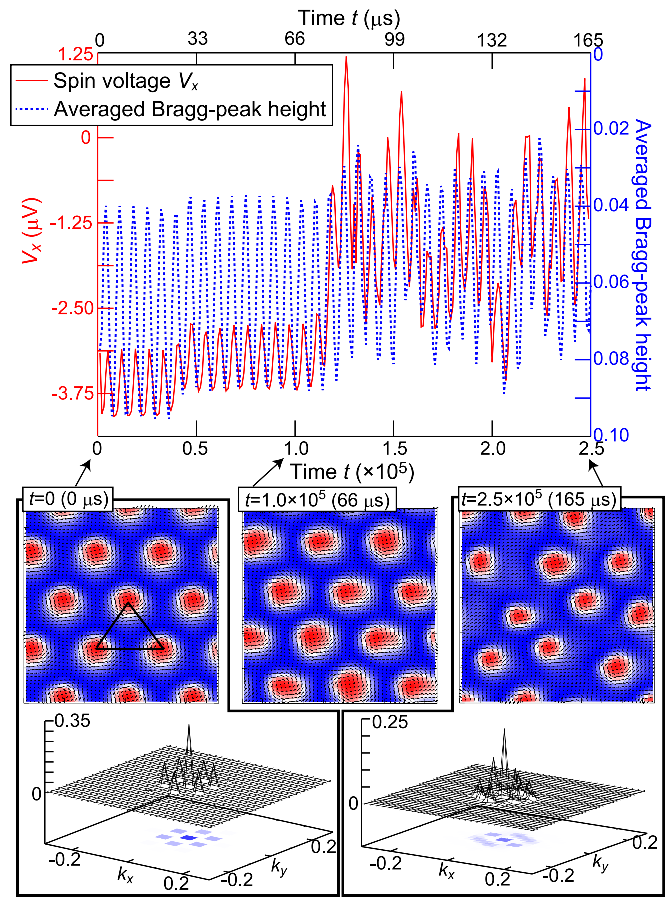

FIG. 7. Time profiles of the spin voltage and the average of six Bragg peaks. Snapshots of the skyrmion-crystal configurations and the Bragg peaks in momentum space at selected moments are also displayed. In the simulations, the skyrmion crystal is continuously excited by an intense in-plane polarized microwave $\boldsymbol{H}^\omega \parallel \boldsymbol{x}$ with $H^\omega = 3 \times 10^{-3}$ and $\omega = 0.04938$ under application of a tilted magnetic field $\boldsymbol{H}_{\rm ex}$ with $\theta = 30^\circ$ and $H_z = 0.036$.

microwaves to a DC electric voltage. Figure 6(a) plots the calculated AC amplitudes of spin voltages V_x^{AC} and V_y^{AC} as functions of the microwave amplitude H^ω for two different spin-wave modes (i.e., the counterclockwise rotation mode and the breathing mode for the in-plane microwave polarization $\boldsymbol{H}^\omega \parallel \boldsymbol{x}$). Figure 6(b) provides an expanded view of the area for small H^ω indicated by the dashed rectangle in Fig. 6(a). The frequency of the applied microwave field is fixed at $\omega = 0.04938$ for the counterclockwise rotation mode, whereas it is fixed at $\omega = 0.0664$ for the breathing mode in the simulations. When the microwave field is weak with small H^ω, the AC amplitude V_μ^{AC} is proportional to H^ω. Deviations from the linear relation appear when H^ω becomes large, as seen above $H^\omega \sim 3 \times 10^{-3}$ in Fig. 6(a). This deviation can be attributed to the distortion of the triangular skyrmion crystal due to the intense spin-wave excitations.

Conversely, Fig. 6(c) shows the DC components of spin voltages V_x^{DC} and V_y^{DC} as a function of H^ω for the two different spin-wave modes. Figure 6(d) again expands the area of small H^ω indicated by the dashed rectangle in Fig. 6(c). Figures 6(c) and 6(d) show that the DC voltages V_μ^{DC} are proportional to the square of H^ω when H^ω is small, whereas a deviation from this scaling law appears again for a strong microwave field with a large H^ω because the triangular array of the skyrmion crystal becomes distorted by the intense spin-wave excitations. Finally, we propose that measurements of the spin voltage may provide a powerful tool to detect several transition phenomena of magnetic skyrmions. It is known that skyrmions exhibit rich structural phase transitions. For example, nonequilibrium triangular-square-lattice structural transitions upon rapid cooling have been observed experimentally [25–28]. Other issues of interest are the melting of a skyrmion crystal due to intense spin-wave excitations [5] and defect formation in a skyrmion crystal during the crystallization [29,30]. We demonstrate that the time profile of spin voltage sensitively varies depending on the spatial configuration of skyrmions in the skyrmion crystal. In Fig. 7, we show a simulated time profile of the spin voltage and that of the average of six Bragg peaks together. Snapshots of the skyrmion-crystal configuration and the Bragg peaks at selected moments are also shown. In the simulations, the skyrmion crystal is continuously excited by an intense in-plane polarized microwave $\boldsymbol{H}^{\omega} \parallel \boldsymbol{x}$ with $H^{\omega} = 3 \times 10^{-3}$ and $\omega = 0.04938$ under application of a tilted magnetic field $\boldsymbol{H}_{\rm ex}$ with $\theta = 30^{\circ}$. With this intense microwave field, the spin-wave amplitude or the circulation radius of skyrmions in the resonantly excited rotation mode exceeds the lattice constant of the skyrmion crystal, which eventually results in the distortion of the triangular skyrmion crystal. We find an apparent correlation between the oscillation fashion of the spin voltage and that of the Bragg peak in their temporal profiles. Although the skyrmion crystal maintains its triangular form for a while after the onset of microwave irradiation, both the spin voltage and the average magnitude of the Bragg peaks oscillate in a steady fashion. On the contrary, when the skyrmion crystal becomes distorted after a sufficient duration of the microwave application, both quantities undergo disordered oscillations. Although further studies are required to determine how to detect the randomness or the degree of disorder of skyrmion crystals via spin-voltage measurements, this technique may spawn a new research field involving nontrivial phase-transition phenomena of magnetic skyrmions, such as jamming transitions, liquid-gas transitions, dynamical structural transitions, and so on, which are issues of future interest.

IV. SUMMARY

To summarize, we theoretically showed that a temporally oscillating spinmotive force and spin voltage with a large DC component can be generated by exciting spin-wave modes of a magnetic skyrmion crystal confined in a two-dimensional magnet under a static magnetic field tilted from the perpendicular direction. The DC component and the AC amplitude of the induced electric voltage are significantly enhanced when the frequency of the applied microwave is tuned to an eigenfrequency of the spin-wave modes.

The results also revealed that the sign of the DC voltage depends on the microwave polarization and on the excited spin-wave mode, which makes it possible to switch the voltage sign by tuning the microwave parameters. Crucially, the periodically aligned skyrmions in a skyrmion crystal work as batteries in series and so can provide a large electric voltage by summing each contribution. The simulations give electric voltages of a few microvolts when using a nanoscopically small system of $\sim$50 $\times$ 50nm^2 containing 12 skyrmions. This indicates that if we use a larger device or sample with a microscopic size rather than a nanoscopic sample, the generated electric voltage should be five or six orders of magnitude greater than that obtained in the present simulations. We also note that the energy ratio of the AC and DC components for the induced spinmotive force can be evaluated by using the formula $2V^{\rm DC}/V^{\rm AC}$, where $V^{\rm AC}/2$ is the effective voltage value for the AC component. According to our calculation results, it takes typically 10%–12% at most. To enhance the efficiency of the microwave-to-DC-voltage conversion, the usage of materials with low dissipations or low damping rates and large microwave absorption coefficient is better.

These findings pave the way to efficient conversion of microwaves to DC electric voltage via skyrmion-hosting magnets, which should be useful in future spintronics devices. Experimental realization and observation of the phenomena predicted here are subjects for future research. It is also worth mentioning that in addition to the skyrmion crystals in quasi-two-dimensional samples studied here, those in three-dimensional bulk samples [31,32], isolated skyrmions in ferromagnetic states [33], and single skyrmions confined in nanodots [34,35] turned out to show peculiar spin-wave modes, and they also exhibit interesting dynamical phenomena and possibly useful microwave-device functions [36–42]. The spinmotive forces due to these microwave-induced spin-wave excitations in different forms of magnetic skyrmions are issues of interest for future studies.

ACKNOWLEDGMENTS

This work was partly supported by JSPS KAKENHI (Grants No. 17H02924, No. 16H06345, and No. 19H00864) and a Waseda University Grant for Special Research Projects (Project No. 2019C-253). We thank J. Ohe, M. Ikka, Y. Ohki, and Y. Shimada for useful discussions.

[1] G. E. Volovik, J. Phys. C **20**, L83 (1987).
[2] S. E. Barnes and S. Maekawa, Phys. Rev. Lett. **98**, 246601 (2007).
[3] S. A. Yang, G. S. D. Beach, C. Knutson, D. Xiao, Q. Niu, M. Tsoi, and J. L. Erskine, Phys. Rev. Lett. **102**, 067201 (2009).
[4] K. Tanabe, D. Chiba, J. Ohe, S. Kasai, H. Kohno, S. E. Barnes, S. Maekawa, K. Kobayashi, and T. Ono, Nat. Commun. **3**, 845 (2012).
[5] M. Mochizuki, Phys. Rev. Lett. **108**, 017601 (2012).
[6] O. Petrova and O. Tchernyshyov, Phys. Rev. B **84**, 214433 (2011).
[7] J. Ohe and Y. Shimada, Appl. Phys. Lett. **103**, 242403 (2013).
[8] Y. Shimada and J. I. Ohe, Phys. Rev. B **91**, 174437 (2015).
[9] P. Bak and M. H. Jensen, J. Phys. C **13**, L881 (1980).
[10] S. D. Yi, S. Onoda, N. Nagaosa, and J. H. Han, Phys. Rev. B **80**, 054416 (2009).
[11] S. Mühlbauer, B. Binz, F. Jonietz, C. Pfleiderer, A. Rosch, A. Neubauer, R. Georgii, and P. Böni, Science **323**, 915 (2009).
[12] A. Tonomura, X. Z. Yu, K. Yanagisawa, T. Matsuda, Y. Onose, N. Kanazawa, H. S. Park, and Y. Tokura, Nano Lett. **12**, 1673 (2012).
[13] N. Nagaosa and Y. Tokura, Nat. Nanotechnol. **8**, 899 (2013).
[14] A. Fert, V. Cros, and J. Sampaio, Nat. Nanotechnol. **8**, 152 (2013).
[15] M. Mochizuki and S. Seki, J. Phys.: Condens. Matter **27**, 503001 (2015).
[16] S. Seki and M. Mochizuki, *Skyrmions in Magnetic Materials*, Springer Briefs in Physics (Springer, Berlin, 2015).

[17] A. N. Bogdanov and D. A. Yablonskii, Sov. Phys. JETP **68**, 101 (1989).
[18] A. Bogdanov and A. Hubert, J. Magn. Magn. Mater. **138**, 255 (1994).
[19] U. K. Rößler, A. N. Bogdanov, and C. Pfleiderer, Nature (London) **442**, 797 (2006).
[20] X. Z. Yu, Y. Onose, N. Kanazawa, J. H. Park, J. H. Han, Y. Matsui, N. Nagaosa, and Y. Tokura, Nature (London) **465**, 901 (2010).
[21] X. Z. Yu, N. Kanazawa, Y. Onose, K. Kimoto, W. Z. Zhang, S. Ishiwata, Y. Matsui, and Y. Tokura, Nat. Mater. **10**, 106 (2011).
[22] S. Seki, X. Z. Yu, S. Ishiwata, and Y. Tokura, Science **336**, 198 (2012).
[23] T. Adams, A. Chacon, M. Wagner, A. Bauer, G. Brandl, B. Pedersen, H. Berger, P. Lemmens, and C. Pfleiderer, Phys. Rev. Lett. **108**, 237204 (2012).
[24] S.-Z. Lin and A. Saxena, Phys. Rev. B **92**, 180401(R) (2015).
[25] K. Karube, J. S. White, N. Reynolds, J. L. Gavilano, H. Oike, A. Kikkawa, F. Kagawa, Y. Tokunaga, H. M. Ronnow, Y. Tokura, and Y. Taguchi, Nat. Mater. **15**, 1237 (2016).
[26] T. Nakajima, H. Oike, A. Kikkawa, E. P. Gilbert, N. Booth, K. Kakurai, Y. Taguchi, Y. Tokura, F. Kagawa, and T. Arima, Sci. Adv. **3**, e1602562 (2017).
[27] H. Oike, A. Kikkawa, N. Kanazawa, Y. Taguchi, M. Kawasaki, Y. Tokura, and F. Kagawa, Nat. Phys. **12**, 62 (2016).
[28] A. Chacon, L. Heinen, M. Halder, A. Bauer, W. Simeth, S. Muhlbauer, H. Berger, M. Garst, A. Rosch, and C. Pfleiderer, Nat. Phys. **14**, 936 (2018).
[29] T. Matsumoto, Y.-G. So, Y. Kohno, H. Sawada, Y. Ikuhara, and N. Shibata, Sci. Adv. **2**, e1501280 (2016).
[30] H. Nakajima, A. Kotani, M. Mochizuki, K. Harada, and S. Mori, Appl. Phys. Lett. **111**, 192401 (2017).
[31] T. Schwarze, J. Waizner, M. Garst, A. Bauer, I. Stasinopoulos, H. Berger, C. Pfleiderer, and D. Grundler, Nat. Mater. **14**, 478 (2015).
[32] M. Garst, J. Waizner, and D. Grundler, J. Phys. D **50**, 293002 (2017).
[33] S.-Z. Lin, C. D. Batista, and A. Saxena, Phys. Rev. B **89**, 024415 (2014).
[34] M. Beg, M. Albert, M.-A. Bisotti, D. Cortés-Ortuño, W. Wang, R. Carey, M. Vousden, O. Hovorka, C. Ciccarelli, C. S. Spencer, C. H. Marrows, and H. Fangohr, Phys. Rev. B **95**, 014433 (2017).
[35] K. Y. Guslienko and Z. V. Gareeva, IEEE Magn. Lett. **8**, 4100305 (2017).
[36] G. Finocchio, F. Büttner, R. Tomasello, M. Carpentieri, and M. Kläui, J. Phys. D **49**, 423001 (2016).
[37] M. Mochizuki and S. Seki, Phys. Rev. B **87**, 134403 (2013).
[38] Y. Okamura, F. Kagawa, M. Mochizuki, M. Kubota, S. Seki, S. Ishiwata, M. Kawasaki, Y. Onose, and Y. Tokura, Nat. Commun. **4**, 2391 (2013).
[39] M. Mochizuki, Phys. Rev. Lett. **114**, 197203 (2015).
[40] Y. Okamura, F. Kagawa, S. Seki, M. Kubota, M. Kawasaki, and Y. Tokura, Phys. Rev. Lett. **114**, 197202 (2015).
[41] W. Wang, M. Beg, B. Zhang, W. Kuch, and H. Fangohr, Phys. Rev. B **92**, 020403(R) (2015).
[42] M. Ikka, A. Takeuchi, and M. Mochizuki, Phys. Rev. B **98**, 184428 (2018).